

pubs.acs.org/JACS Article

Tunneling-Driven Marcus-Inverted Triplet Energy Transfer in a Two-Dimensional Perovskite

Angana De, Carlos Mora Perez, Aihui Liang, Kang Wang, Letian Dou, Oleg Prezhdo, and Libai Huang*



Cite This: J. Am. Chem. Soc. 2024, 146, 4260-4269



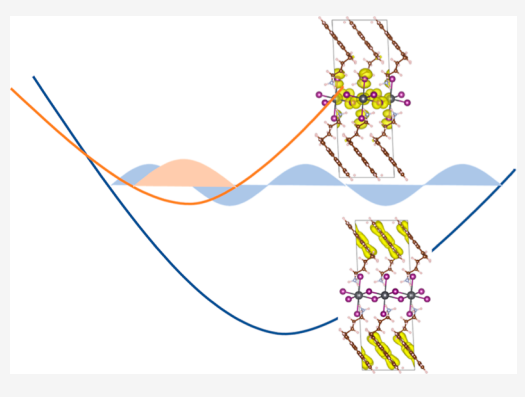
ACCESS

III Metrics & More

Article Recommendations

Supporting Information

ABSTRACT: Quantum tunneling, a phenomenon that allows particles to pass through potential barriers, can play a critical role in energy transfer processes. Here, we demonstrate that the proper design of organic—inorganic interfaces in two-dimensional (2D) hybrid perovskites allows for efficient triplet energy transfer (TET), where quantum tunneling of the excitons is the key driving force. By employing temperature-dependent and time-resolved photoluminescence and pump—probe spectroscopy techniques, we establish that triplet excitons can transfer from the inorganic lead-iodide sublattices to the pyrene ligands with rapid and weakly temperature-dependent characteristic times of approximately 50 ps. The energy transfer rates obtained based on the Marcus theory and first-principles calculations show good agreement with the experiments, indicating that the efficient tunneling of triplet excitons within the Marcus-inverted regime is facilitated by high-frequency molecular vibrations.



These findings offer valuable insights into how one can effectively manipulate the energy landscape in 2D hybrid perovskites for energy transfer and the creation of diverse excitonic states.

1. INTRODUCTION

A key objective in designing hybrid materials for energy harvesting and light-emitting applications is efficient energy transfer across organic-inorganic interfaces. 1-10 Triplet energy transfer (TET) is a crucial and often the rate-determining step in processes such as photon upconversion and phosphorescence-based light-emitting diodes. TET generally occurs through the Dexter mechanism, which involves a simultaneous transfer of electrons between donor and acceptor entities. 11-14 The electronic states of the donor and acceptor are assumed to have the same spin multiplicity. Compared to Förster resonance energy transfer (FRET), which is enabled by longrange dipole-dipole interactions, TET is usually much slower—occurring on the 100 s of ns or longer time scales in molecular systems. 12 In recent years, there has been an upsurge of interest in hybrid organic-inorganic systems, such as chalcogenide and halide perovskite quantum dots with designed triplet acceptor ligands, for efficient energy upconversion. ^{1-5,15-19} In these systems, the inorganic semiconductors are utilized as sensitizers or donors. Spin-orbit coupling in the inorganic semiconductors reduces the exchange splitting between their singlet and triplet excited states, thereby optimizing the generation of triplet excitons in these structures. However, TET at the interfaces between quantum dots/3D metal halide perovskites and organic ligands is still relatively slow, occurring over time scales of tens of nanoseconds to hundreds of microseconds. 1,3,4,7-9,15-17

Two-dimensional (2D) hybrid organic-inorganic perovskites offer a new platform for controlling interfacial energy landscapes and electronic couplings, thereby promoting efficient charge and energy transfer processes. 10,21-26 Excitons confined in the inorganic lattices, which are strongly bound with binding energies as large as 400 meV, feature a large oscillator strength. Uniquely, wave function hybridization can occur between the frontier orbitals of the organic ligands and inorganic lattices, resulting in theoretically predicted Dexter electronic couplings as large as 40 meV.²³ In addition, large spin-orbit coupling facilitated by the inclusion of heavy elements like Pb is beneficial for enhancing phosphorescence from the organic ligand. 10 Recently, investigations into TET from the inorganic sublattice to the organic ligands in 2D perovskites have demonstrated remarkably fast transfer times on the picosecond time scale. 21,24,25 These TET rates are significantly faster than those observed at the interfaces of quantum dots/3D perovskites and molecular acceptors, pointing toward the immense potential of 2D perovskites. However, the detailed mechanism underpinning the fast TET at these interfaces remains elusive. Specifically, temperaturedependent behavior, which is essential for mechanistic understanding, has yet to be comprehensively explored. The

Received: January 6, 2024 Revised: January 16, 2024 Accepted: January 18, 2024 Published: February 2, 2024





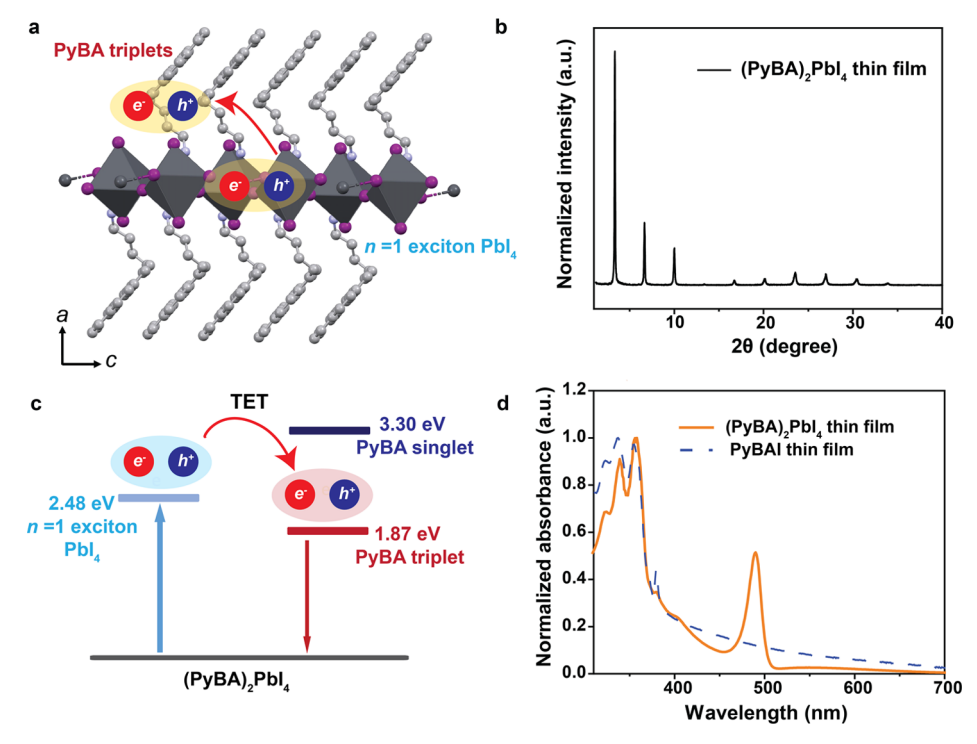


Figure 1. Structural characterization and band alignment. (a) Schematic structure of $(PyBA)_2PbI_4$ —the n=1 2D perovskite with pyrene-based PyBA ligands and (b) powder XRD pattern of the $(PyBA)_2PbI_4$ thin film. (c) Relative exciton energy levels of the lead-iodide (donor) and pyrene (acceptor) layers of $(PyBA)_2PbI_4$, showing the energetic feasibility of TET across the inorganic—organic interface. (d) UV—vis absorption spectra of thin films of the PyBA ligand (dashed blue line) vs that of the n=1 2D perovskite (solid orange line).

underlying mechanisms are pivotal for the successful application of materials-by-design principles in the realm of 2D hybrid perovskites.

In this work, we investigate the TET at organic-inorganic interfaces using temperature-dependent and time-resolved photoluminescence (TRPL) and transient absorption spectroscopy. We employed a 2D lead-iodide perovskite with a pyrene-based organic cation as our model system because the triplet excitons in pyrene are highly emissive. 14,20,27-29 We observed efficient TET occurring across this 2D hybrid organic-inorganic interface, resulting in pyrene phosphorescence. By modeling the temperature-dependent TET, we concluded that the TET process falls in the inverted Marcus domain and is driven by quantum mechanical tunneling. Strong electronic coupling leads to orders of magnitude faster TET time of tens of picoseconds, as compared to other hybrid systems that have been studied in this regard. Tunneling also strongly diminishes the temperature dependence of the TET rate. Our work illustrates the opportunities of rationally designing the energy landscape between the donor and acceptor species in 2D materials for efficient energy transfer applications.

2. RESULTS AND DISCUSSION

2.1. Structure and Energy Band Alignment of 2D Perovskites. The pyrene-based organic ligand, 4-(pyren-1-yl)butan-1-ammonium iodide [PyBAI, $C_{16}H_{10}$ -(CH_2)₄-NH₃I], was prepared through a multistep synthesis following a published procedure (more details in Methods and Figure S1)³⁰ and characterized via NMR spectroscopy (Figure S2), as detailed in Sections S1.1 and S1.2 in the Supporting Information. We chose pyrene as the triplet exciton acceptor because its triplet state lies energetically below the conduction

band of the lead-iodide sublattice (donor) and due to the high efficiency of its phosphorescence. 3,20,27,28 The thin films of the n=1 and n=2 2D perovskites, $(PyBA)_2PbI_4$ and $(PyBA)(FA)_2Pb_2I_7$, respectively, were then synthesized by a solution-based method (FA refers to as formamidine, see Methods for detailed information). Figure 1a shows the schematic crystal structure of $(PyBA)_2PbI_4$. The powder XRD pattern of the n=1 perovskite film shows sharp peaks that indicate a reasonable degree of crystallinity and phase purity of the sample (Figure 1b). The approximated energy levels of the n=1 and n=2 2D perovskites were determined in an earlier work, using ultraviolet photoelectron spectroscopy as elaborated in Section S2 of the Supporting Information, and are summarized in Table S1.

As shown in Figure 1c, the triplet state of pyrene lies below the n = 1 exciton resonance, and TET across the inorganic organic interface is energetically feasible ($\Delta E \sim 0.6$ eV). The CBM of the inorganic layer is also slightly above the triplet LUMO $(\Delta E \sim 0.2 \text{ eV})^{22,31}$ of pyrene, thus electron transfer from the lead-iodide sublattice to the pyrene-based ligand (PyBA) is also possible. On the other hand, the n = 1 exciton lies below the singlet state of the organic ligand. As depicted in Figure 1d, the peaks observed around 337 and 358 nm in the UV-vis absorption spectra of both (PyBA)₂PbI₄ and PyBAI thin films originate from singlet excitons in the pyrene-based ligand.³² The distinctly sharp peak at 490 nm, present only in the case of (PyBA)₂PbI₄, is attributed to the absorption of the n=1 exciton residing in the $[PbI_4]^{2-}$ inorganic layer of the perovskite. As shown in Figure S3, the negligible overlap between the emission spectrum of the n = 1 exciton and the absorption spectrum of PyBA establishes that the possibility of singlet energy transfer from PbI₄²⁻ to pyrene through a Förster mechanism is low.

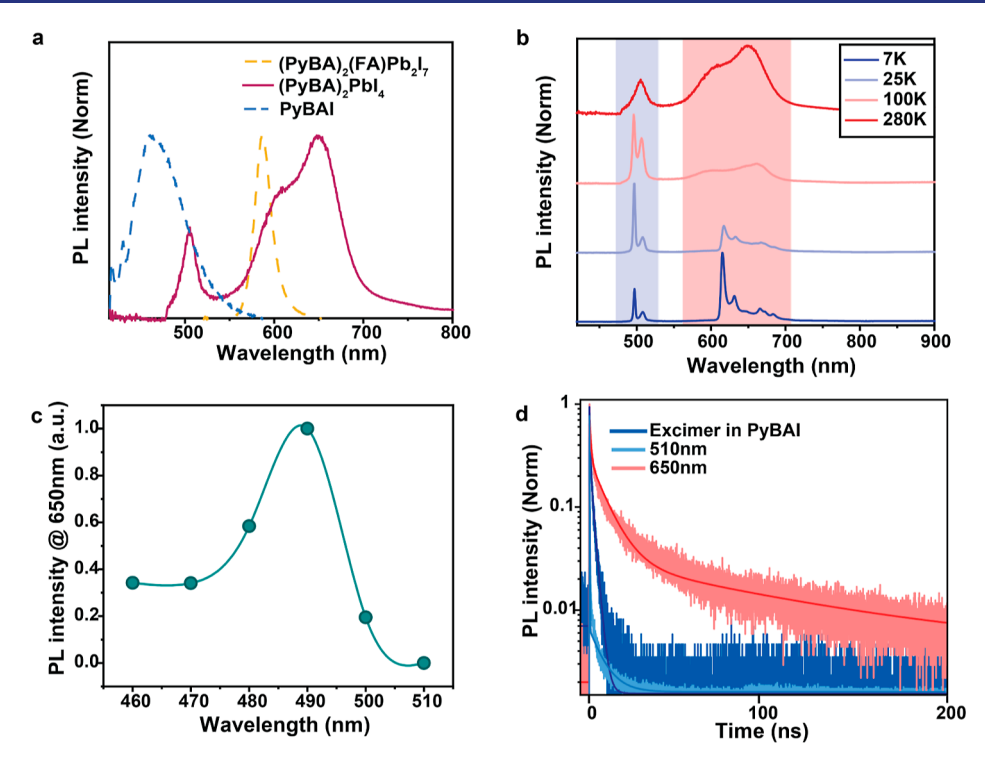


Figure 2. Triplet emission and lifetimes. (a) Emission spectra at room temperature ($\lambda_{EX} = 447 \text{ nm}$) of thin films of the pyrene ligand (PyBAI) vs the n = 1 and n = 2 2D perovskites, which show pyrene phosphorescence only in the case of the n = 1 perovskite, (PyBA)₂PbI₄. (b) Temperature-dependent PL spectra ($\lambda_{EX} = 447 \text{ nm}$) of (PyBA)₂PbI₄, which shows the sharp peaks of pyrene phosphorescence centered around 650 nm at low temperatures evolving into a broad emission at 280 K. (c) Photoluminescence excitation (PLE) spectrum of (PyBA)₂PbI₄, monitoring the emission intensity of the pyrene phosphorescence (\sim 650 nm) while varying the excitation wavelength. (d) TRPL dynamics of (PyBA)₂PbI₄ taken at 280 K along with the fits to multiexponential decays (Table S3), which shows the longer lifetime of triplet excitons in pyrene, as compared to the n = 1 Wannier exciton in the Pb–I layer and the singlet excimers in the pure PyBAI film.

As depicted in Figure 2a, the PL spectrum of a thin film of PyBAI shows a broad emission centered at 470 nm which arises from singlet excimers of pyrene.^{33,34} This is in sharp contrast to the PL spectrum of (PyBA)₂PbI₄, which shows an emission peak at 500 nm arising from the n = 1 inorganic exciton in the PbI₄²⁻ layer and a more intense, red-shifted emission centered at 650 nm. Given the triplet state of pyrene lies around 1.87 eV,³¹ we attribute the emission near 650 nm to phosphorescence from the triplet excitons in pyrene ligands. As a control, we also fabricated $(PyBA)_2(FA) Pb_2I_7$, the n = 2perovskite-in which the thicker inorganic layer causes an increased screening of the n = 2 Wannier exciton. As shown in Figure S4, this results in a red shift of the n = 2 excitonic absorption and a reduction in the band gap of the lead-iodide layer.²² Therefore, the resulting band alignment between the organic and inorganic layer in the n = 2 2D perovskite is no longer favorable for TET, and phosphorescence from pyrene is absent in this material, as shown in Figure 2a.

Next, we performed temperature-dependent PL measurements on $(PyBA)_2PbI_4$ (Figure 2b), and a much narrower and more structured emission at around 650 nm was observed as the temperature decreases. These sharp peaks at \sim 650 nm are vibronic resonances of the localized triplet excitons and have been well-documented previously for pyrene. ^{27–29,31} Furthermore, we can exclude the possibility that traps or defects contribute to these emissions. Emissions stemming from trapped excitons or other defect states in 2D perovskites typically display much broader spectral profiles and do not exhibit the sharp vibrational features that we observe, even when measured at low temperatures. For example, a recent

publication shows much broader trap emission at low temperature compared to the triplet emission at room temperature in 2D perovskites containing naphthalene-derived ligands.³⁵ In addition, as shown in Figure S5, subgap excitation renders negligible emission, again confirming that the emission is not originated from subgap states. These sharp features evolve into a broader emission at higher temperatures, likely due to the formation of triplet excimers.³⁶ To confirm energy transfer, we conducted PLE experiments on (PyBA)₂PbI₄, where the emission intensity from the phosphorescence at 650 nm was monitored while varying the excitation wavelength. The overlap of the PLE spectrum (Figure 2c) with the absorption maxima of the n = 1 inorganic exciton at 490 nm clearly indicates that phosphorescence occurs following energy transfer from the Wannier excitons in [PbI₄]²⁻ to the triplet states in the pyrene ligands. In contrast, the PyBAI thin film exhibits negligible emission under 490 nm excitation (Figure S6). At low temperatures, the n = 1 excitonic peak split into two peaks. Such splitting in the Pb-based 2D perovskites may arise from Rashba splitting induced by strong spin-orbit coupling,³⁷ or due to an enhanced electron-hole exchange interaction in these materials.³⁸ Alternatively, other theories suggest that it could result from exciton polarons³⁹ and dark excitons.40

This assignment of the $\sim\!650$ nm emission to phosphorescence from the pyrene ligands is also supported by the TRPL dynamics measured by time-correlated single-photon counting (TCSPC) (Figures 2d and 3a). At room temperature, the decay of the emission at 650 nm can be fit to a triexponential curve, whose longest component is 98.5 ± 2.1 ns. This is much

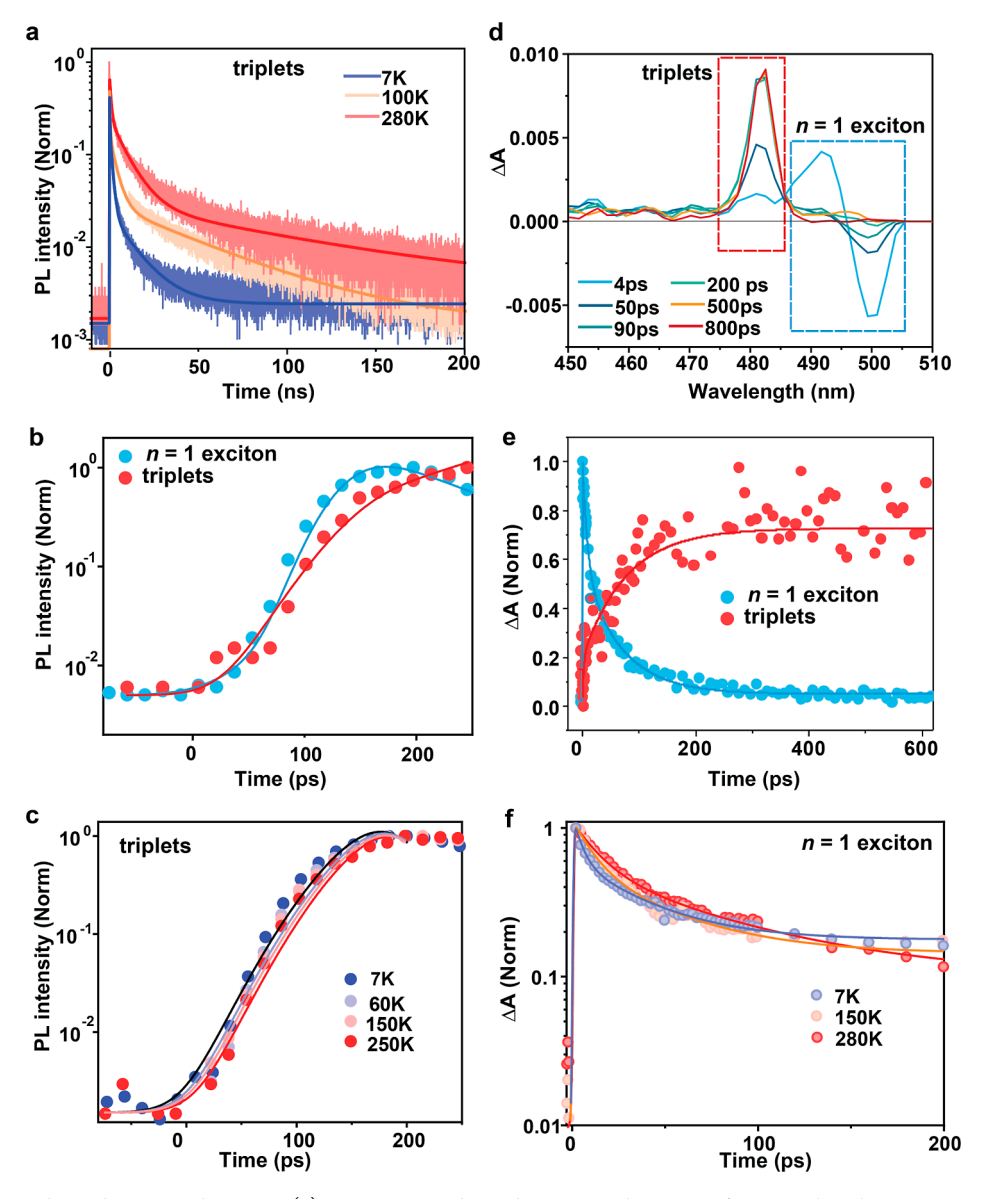


Figure 3. Temperature-dependent TET dynamics. (a) Temperature-dependent TRPL dynamics of pyrene phosphorescence in $(PyBA)_2PbI_4$ along with fits to triexponential decay excited at 447 nm, which show an increase in the lifetime of the pyrene triplets at elevated temperatures. (b) TRPL dynamics at 200 K of the first 200 ps, depicting a much slower rise/growth of the triplet population in pyrene through TET, as compared to that of the n = 1 Wannier excitons formed by direct excitation of Pb–I. (c) Temperature-dependent rise times of the pyrene phosphorescence, which demonstrate a weak dependence of the TET rate on T. Solid lines are fits to an exponential rise convoluted with a Gaussian response function. (d) Transient absorption spectra of the $(PyBA)_2PbI_4$ film at indicated time delays, followed by selective excitation of PbI₄. (e) TA kinetics of the n = 1 exciton (~500 nm) and pyrene triplets (~480 nm). The solid lines are fits to exponential functions. The growth of the triplets is fitted with a single exponential rise with a time constant of 70 ± 10 ps and the decay of the n = 1 excitonic resonance is fitted with a biexponential decay of 8.7 ± 1.1 ps (45%) and (67 ± 5) ps (55%). (f) Temperature-dependent TA kinetics of the n = 1 Wannier exciton decay in the PbI₄²⁻ layer, which show slower decays at higher temperatures. The solid lines are fits to a biexponential decay (parameters in Table S5).

longer than the lifetimes of the n=1 Wannier exciton at 510 nm in the lead-iodide layer, as well as that of the singlet excimers (at ~470 nm) observed in the pure PyBAI film. The fitting parameters are summarized in Table S2. The multi-exponential nature of the triplet decay can be attributed to nonradiative processes, for example, triplet back transfer and trapping. This idea is further supported by the low quantum yield (~0.1%) of the phosphorescence (Figure S7). Fluence-dependent measurements (Figure S8) show negligible variation in the triplet decay dynamics with excitation fluences below 1.4 mJ/cm². We employed a fluence of 20 μ J/cm² for data shown in Figures 2 and 3, thus ruling out the contribution of triplet—triplet annihilation.

The long lifetimes of these triplet excitons at room temperature lead to the slightly sublinear dependence of their PL on excitation fluences $\propto I^{0.9}$, due to saturation effects, where I is the laser intensity. In contrast, the n=1 inorganic exciton shows a linear power dependence (Figure S9). As the temperature decreases, the phosphorescence lifetime shortens to 13.6 ± 0.8 ns at 7 K (Figure 3a). The fittings for the temperature-dependent TRPL kinetics of pyrene phosphorescence are summarized in Table S3. We propose that the prolonged phosphorescence lifetime at higher temperatures is attributed to the transformation of pyrene triplets into a triplet-excimer-like state. This is supported by the broad, featureless emission observed at room temperature,

in contrast to the structured emission at 7 K (Figure 2b). The temperature dependence of the triplet lifetime contradicts the behavior expected from emissions associated with trap states, as elevated temperatures typically result in the detrapping of excitons, leading to a reduction in lifetime. We note that the lifetime of the phosphorescence here is shorter than that observed in pyrene crystals.³¹ This can be explained by the close proximity of the pyrene molecules to the Pb-I lattices, which leads to an enhanced radiative rate of the triplet excitons in pyrene, induced by the heavy-atom effect.²⁸ The incorporation of I in the inorganic layer, along with Pb can substantially reduce phosphorescence lifetimes by more than an order of magnitude. For example, in dinuclear Ir₂I₂ complexes, phosphorescence lifetimes as short as 50 ns have been reported, which is in stark contrast to halide-free Ir(III) complexes with phosphorescence lifetimes in the range of hundreds of nanoseconds. 42 Multiexponential triplet decay with fast component on the ns time scale has also been reported recently in 2D halide perovskites containing naphthalene-derived cations. 35,43

2.2. Weak Temperature Dependence of TET. To extract the TET time, we monitored the rise in triplet emission from the pyrene ligands at 650 nm. As shown in Figure 3b, the growth of triplet emission is slower than that of the PL from the directly excited n = 1 Wannier excitons. The rise time of pyrene phosphorescence is estimated by fitting its TRPL dynamics using a convoluted exponential rise function with a Gaussian response function (Table S4).

These results reveal that TET occurs over a time scale of 65.0 ± 5.7 ps at 200 K (Figure 3b). Remarkably, as shown in Figure 3c, the TET rate is only weakly temperature-dependent over a large range of temperatures (7–250 K) and is, in fact, slightly higher at lower temperatures (for example, the TET time scale is 49.9 ± 4.1 ps at 7 K). We note that Ema et al. made a similar observation of temperature-dependent energy transfer in their work in naphthalene-based 2D perovskites; however, the underlying reason was not elucidated in detail. 21

To directly probe the formation of the triplets, we performed transient absorption (TA) spectroscopy measurements with a temporal resolution of ~200 fs (Figure 3d). Upon selectively exciting the PbI₄²⁻ layer of the perovskite, a sharp bleach can be observed at ~500 nm originating from the n = 1 exciton in the inorganic layer. The n = 1 exciton resonance decays simultaneously with the emergence of a distinct long-lived excited-state absorption (ESA) signal at \sim 480 nm (Figure 3d). We assigned the long-lived ESA to T_1 – T_n absorption, which overall agrees with the spectra from sensitized triplets (Figure S10). A prior study on the triplets of pyrene carboxylic acid ligands on CdSe quantum dots² revealed a triplet absorption peak at 430 nm with a shoulder at ~480 nm. We observed only a peak at 480 nm but not at 430 nm in the ESA band of PyBA. This discrepancy could be attributed to our spectral response being limited to below 450 nm. Additionally, the shift in the triplet absorption energy might also be a consequence of the absence of electronegative atoms in PyBA, which could influence the energy levels.⁴⁴ The triplet ESA grows with a single-exponential rise of 70 ± 10 ps, aligning with the slow decay (67 \pm 5 ps, 55% weight) of the n = 1 excitons (Figure 3e) as well as the rise time $(67.2 \pm 7.6 \text{ ps})$ of the phosphorescence at 250 K. This observation supports the occurrence of a concerted TET mechanism. To further elucidate the dependence of the n = 1 exciton decay on temperature, we compared the dynamics obtained at 7, 150,

and 280 K (Figure 3f). Fluence-dependent dynamics show no change in the decay kinetics of the n=1 exciton in the range of excitation powers used for pump—probe measurements, thus, eliminating the occurrence of nonlinear effects such as Auger recombination (Figure S11). The slow component of the n=1 excitons becomes slightly faster at lower temperatures (ranging from 53.7 ± 3.0 ps at 7 K to 70.0 ± 0.1 ps at 280 K) and mirrors the trend observed in the rise time of the triplet formation, which provides additional support for a concerted TET mechanism. The kinetic fittings of the n=1 excitons at different temperatures are summarized in Table S5.

In contrast, in the sequential mechanism, the triplet forms in two steps, with the hole transfer following the electron transfer (or vice versa). 15,25 In such a scenario, the charge transfer (CT) state will serve as an intermediate for triplet formation, and thus, the decay of the CT state should directly correlate with the rise of the triplet state. As discussed earlier, electron transfer from PbI₄²⁻ to triplet LUMO is also possible. The decay of the n = 1 exciton has an additional fast component of 8.7 ± 1.1 ps (45% weight), which is consistent with the ~10 ps CT across organic-inorganic interfaces in 2D perovskites with conjugated ligands in our previous work.⁴⁵ As shown in Figure \$12a, we also observed a broad absorption band at ~530-600 nm that persists over 100 s of ps, which agrees well with the absorption of the CT state observed previously.⁴⁵ We tentatively assigned this broad absorption band to the CT state, resulting from electron transfer from PbI₄²⁻ to PyBA ligands. The slow decay of this CT state, occurring at 100 s of ps (Figure S12b), implies that the sequential mechanism would lead to a slower TET time scale of 100 s of ps. Given the sequential mechanism is likely to occur on a much slower time scale, we conclude that a concerted mechanism plays a more dominant role. Nevertheless, the possibility of a sequential mechanism contributing to TET cannot be completely ruled

It should also be considered that the absorption of pyrene radical ions might contribute to the ESA at ~480 nm. 46 If the observed ESA feature at this wavelength were primarily due to pyrene radical ions resulting from CT, the rise time of the triplet emission, which is about 70 ps as determined by TRPL measurements, would be expected to correspond with the decay of the 480 nm band. However, our observations do not support this; the ESA feature shows practically no decay within the 600 ps time frame, as seen in Figure 3e. Consequently, we concluded that the TA feature at 480 nm was not predominantly derived from the pyrene radical ions but was more likely attributed to triplet absorption. We estimated the quantum yield of the TET processes by QY $_{\rm TET} = \frac{\kappa_{\rm ET}}{k_{\rm r} + k_{\rm ar} + k_{\rm ET}}$ where $k_{\rm ET}$ is the TET rate, and $k_{\rm r}$ and $k_{\rm nr}$ are the radiative and nonradiative lifetimes of the n = 1 exciton. Given that the electron transfer to the ligands primarily occurs on the picosecond time scale, it is the main contribution of k_{nr} . By assuming that $k_{\rm r}$ is much slower, we can estimate ${
m QY}_{
m TET}$ at room temperature to be ~11% based on the electron transfer and TET times of 9 and 70 ps, respectively.

2.3. Tunneling-Driven TET. The weak temperature dependence of the TET rate is intriguing because it indicates that quantum tunneling is the main driving mechanism. ^{47,48} This weak temperature dependence is in contrast to the classical Marcus theory which, in the absence of quantum tunneling, typically necessitates overcoming an energetic barrier for TET. This barrier leads to reduced transfer rates

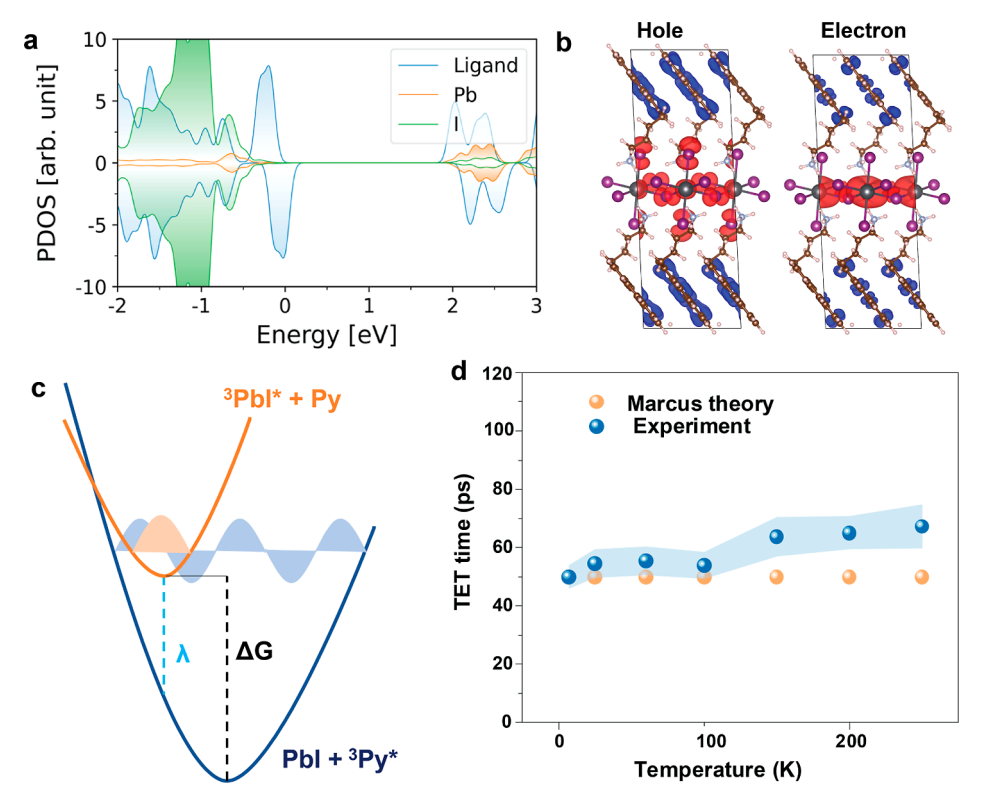


Figure 4. Quantum-tunneling-driven TET. (a) Spin-polarized projected density of states (PDOSs) for the (PyBA)₂PbI₄ system with the charge densities of the initial TET orbitals localized in the lead-iodide layer. (b) Charge density difference between the final and initial orbitals of hole (left) and electron (right) involved in TET. Red represents the initial orbitals localized onto the [PbI₄]²⁻ perovskite core, while blue represents the final orbitals localized onto the pyrene molecular layer. (c) Schematic of the Gibbs free energy surfaces as a function of the nuclear configuration of TET from Pb–I to pyrene in the Marcus-inverted regime ($\lambda < -\Delta G^{\circ}$), depicting the enhanced vibrational overlap between the donor and acceptor wave functions. (d) Plot showing the theoretically predicted (orange) and experimentally extracted (blue) TET time scales as a function of temperature, depicting the tunneling-induced weak T dependence of the triplet transfer rate. The shaded blue area indicates the experimental uncertainties in determining the TET times.

at lower temperatures unless the process is barrier-less. ¹⁵ However, in the semiclassical Marcus framework that includes quantum tunneling, one can observe transfer rates that exhibit only a weak dependence on temperature. Such a shallow temperature dependence has been previously attributed to quantum tunneling, notably including CT in photosynthetic reaction centers and molecular junctions. ^{49,50}

In order to understand the energy landscape for interfacial TET, we utilized density functional theory (DFT),51,52 employing both projector-augmented-wave (PAW) potentials⁵³ and the Perdew-Burke-Ernzerhof (PBE) functional^{4,42} to compute the electronic energy levels present in the initial and final states of the energy transfer process (Figures 4a,b and S13-S17). The initial excitation is near the band edge of the Pb-I core (see the PDOSs in Figures 4a and S16-S17). TET occurs downward in energy, and the final state is the triplet of the pyrene layer. The initial (red color) and final orbitals (blue color) of the hole and electron undergoing concerted transfer during the TET process are shown in Figure 4b. Initially, the excitation is localized on the [PbI₄]²⁻ layer, while after TET, the excitation is on the pyrene layer. The Marcus theory calculations for the TET process reveal that the magnitude $-\Delta G^{\circ}$ (0.835 eV), the Gibbs free energy change for the reaction (see Table S6), is greater than that of reorganization energy λ (0.564 eV) (see Table S7), thereby placing this material in the Marcus-inverted domain (Figure 4c). In classical Marcus theory (Section S4.1), a barrier dictated by λ and ΔG° , $(\lambda + \Delta G^{\circ})$, has to be overcome energetically,

which leads to a slower transfer rate as temperature decreases in both normal and inverted regimes. 54,54,55,55 The TET time scales, as predicted by classical Marcus theory, are plotted in Figure S18. Clearly, these TET times are many orders of magnitude slower than what is observed experimentally, and the exponential dependence of the transfer rate on temperature also contradicts the trends extracted from our TRPL and TA studies.

Thus, we consider the semiclassical picture with a contribution from quantum tunneling, which occurs due to the overlap of the vibrational wave functions of the donor and acceptor species. The DFT calculations show that the organic ligands undergo more significant geometric changes than the inorganic sublattice. The root-mean-square displacements of [PbI₄]²⁻ and pyrene are 0.05 and 0.68 Å, respectively. This is because organic molecules are less rigid than the inorganic sublattice and tend to distort more substantially upon excitation. Thus, the Marcus theory reaction coordinate (Figure 4c) is largely attributed to the pyrene ligands. Vibrational frequencies of organic ligands are much higher than those of the lead-iodide lattice composed of heavy elements. The vibrational energy is sufficiently high to prevent the onset of thermally activated processes, even at room temperature. As a result, TET occurs efficiently via tunneling through the relatively narrow barrier in the Marcus-inverted region.

At the low-temperature $(k_{\rm B}T < \hbar\omega)$ tunneling regime, the TET rate is described in Marcus theory by the following rate expression ^{56,57}

$$k_{\rm ET} = 1/\hbar \frac{2\pi H_{12}^2}{\hbar \omega} \exp \left(\frac{\Delta G^{\circ}}{\hbar \omega} \ln \frac{e\lambda}{|\Delta G^{\circ}|} \frac{\lambda}{\hbar \omega} \right)$$

We employed a value of 1500 cm⁻¹ for the vibrational frequency, ω , roughly corresponding to a carbon-carbon stretch. The electronic coupling between the inorganic and organic layers, H_{12} , was estimated to be on the order of 10 meV, which aligns well with ref 23. This gives a 50 ps temperature-independent TET time scale, providing good agreement with the experimental data in the 7-295 K temperature range (Figure 4d). One can conceptualize the system oscillating within the Marcus parabola, where tunneling through the barrier during each attempt has a small probability. The TET rates reflect the necessity for numerous tunneling attempts before the system successfully traverses the barrier. H_{12}^2 , ΔG° , and λ were assumed to be temperature-independent in our model. However, these parameters might vary with temperature changes due to alterations in the molecular configuration. Such variations could be responsible for the observed slight decrease in the TET rates at higher temperatures.

2.4. Discussion and Conclusions. Our findings highlight the unique opportunities that 2D hybrid organic-inorganic perovskites offer for the strategic design of energy transfer between conjugated organic ligands and inorganic lattices. The enhanced overlap between the vibrational wave functions of the donor and acceptor layers—induced by their dimensionality and relative band alignment—prompts triplet excitons to tunnel from the inorganic layer to the organic layer, bypassing the need to thermally overcome the potential barrier of the transfer. This mechanism results in remarkably fast, TET time scales of 50-70 ps across a range of 7-295 K. These triplet transfer times are more than 2 orders of magnitude faster than at the interfaces between bulk perovskites and rubrene molecules,9 which presumably have much smaller orbital overlap and hence weaker Dexter-type electronic coupling. TET observed here is also more than 3 orders of magnitude faster than at the interfaces of CdSe and PbS quantum dots, where transfer times on the order of 100 ns have been reported.4,18

The energy landscape of the Marcus-inverted regime plays a crucial role in facilitating triplet exciton tunneling. While the Marcus-inverted regime has been more commonly observed in CT processes, this study reports triplet exciton transfer occurring within the inverted regime that has been much less explored. Experimental observation of Marcus-inverted phenomena can be hindered due to the dominance of parasitic processes such as Auger-assisted transfer, 58 in which the excess driving force is transferred to another excitation or charge, rather than vibrations. This work demonstrates that proper alignment of the donor and acceptor bands, as well as tuning the donor-acceptor coupling, can provide control over the Marcus regime of energy transfer processes in low-dimensional materials. This revelation lays the groundwork for further investigation of Marcus-inverted phenomena in other 2D perovskites and optimization of this class of excitonic materials for designing triplet emissions.

3. METHODS

3.1. Thin Film Preparation. The n=1 perovskite thin film was developed by spin-coating 2:1 molar ratios of the pyrene butyl ammonium iodide salt: lead(II) iodide (Sigma-Aldrich) dissolved at a concentration of 0.3 M (with respect to the organic salt, at 50 °C with constant stirring) in DMF onto freshly cleaned SiO₂ wafers at 2000 rpm for 20 s. The films were then annealed on a hot plate for 15 min at 150 °C.

The n=2 perovskite thin film was developed by spin-coating 2:2:1 molar ratios of the pyrene butyl ammonium iodide salt/lead(II) iodide (Sigma-Aldrich)/formamidinium iodide (Greatcell Solar) dissolved at a concentration of 0.3 M (with respect to the organic salt, at 50 °C with constant stirring) in DMF onto freshly cleaned SiO₂ wafers at 3000 rpm for 60 s. The films were then annealed on a hot plate for 2 min at 180 °C.

The above thin films were characterized by out-of-plane X-ray diffraction (Rigaku SmartLab using a Cu K α source of $\lambda=1.54056$ Å in Bragg–Brentano mode), ultraviolet–visible absorption spectroscopy (Agilent Cary 60 ultraviolet–visible light spectrophotometer), and the other optical measurements discussed in the paper.

3.2. Steady-State and Time-Resolved PL Measurements. A custom-built confocal microphotoluminescence setup was employed for both steady-state and time-resolved optical measurements. We utilized a 447 nm picosecond pulsed diode laser (LDH-P-C-450B, PicoQuant) with a full width at half-maximum of 50 ps and a repetition rate of 5 MHz as the excitation source. This laser was focused onto the sample surface by using a 40× Nikon objective with a numerical aperture (NA) of 0.6. The emitted luminescence was collected via the same objective, dispersed through an Andor Technology monochromator, and subsequently detected by an Andor Shamrock 3030i spectrometer and Newton 920 CCD. An optical filter was strategically placed before the detector to eliminate excitation scatter. For TRPL measurements, we employed a singlephoton avalanche diode (PicoQuant, PDM series) coupled to a single-photon counting module (PicoQuant). Unless otherwise specified, we used a low excitation fluence of 130 nJ/cm² to mitigate the initiation of undesirable bimolecular processes such as excitonexciton annihilation.

For temperature-dependent PL measurements, a Cryostation s50 closed-cycle optical cryostat from Montana Instruments was used. The sample was secured on the holder, and vacuum was established within the sample chamber. This setup allowed us to achieve temperatures ranging from 7 to 295 K, with a temperature stability of better than 10 mK.

Measurements with an excitation wavelength of 490 nm (to selectively excite [PbI₄]²⁻, Figure S6) were conducted by a pump that was the output of an optical parametric amplifier (OPA; TOPASTwins, LIGHT CONVERSION Ltd.) pumped by a high-repetition rate amplifier (750 kHz, PHAROS, LIGHT CONVERSION Ltd.).

- **3.3. Pump**—**Probe Spectroscopy.** The output from a high-repetition rate amplifier (750 kHz, PHAROS, LIGHT CONVERSION Ltd.) was used to pump two independent OPAs (TOPASTwins, LIGHT CONVERSION Ltd.). One OPA generated the pump beam, while the other provided the probe beam. A mechanical translation stage (DDS600-E, Thorlabs) was utilized to introduce a time delay between the pump and probe beams. Both beams were focused onto the sample by using a 40× Nikon objective with an NA of 0.6. The probe beam was collected using the same Nikon objective and then detected by an avalanche photodiode (C5331-04, Hamamatsu). For temperature-dependent pump—probe experiments, we employed a Cryostation s50 from Montana Instruments, allowing us to conduct studies in a high-vacuum environment across a temperature range of 7–295 K.
- **3.4. Computational Methodology.** DFT^{51,52} with the PAW potentials⁵³ and the PBE functional^{59,60} was employed for all systems. The electronic structure calculations were performed within the Vienna ab initio simulation package (VASP).^{61–63} The PAW PBE versions included in the POTCAR files for each species were PAW PBE I 08Apr2002, PAW PBE N 08Apr2002, PAW PBE H

15Jun2001, PAW PBE C 08Apr2002, and PAW PBE Pb 08Apr2002. The 2D perovskite n = 1 (PyBA)₂PbI₄ models were taken from experiment as characterized by out-of-plane X-ray diffraction (see Methods). During the VASP calculations, we utilized a sizable planewave basis energy cutoff of 520 eV, a 5 \times 5 \times 5 Γ centered k-point mesh to sample the Brillouin zone (creating 39 irreducible k-points), and van der Waals dispersion interactions within the Grimme D3 method⁶⁴ for all the full-pyrene system simulations. See Figure S14 for the crystal structure of the (PyBA)₂PbI₄ model. The specific spin multiplet of the system was controlled through the NUPDOWN tag within the INCAR file of the VASP simulation, to set the difference between the number of electrons in the spin-up and spin-down channels (Singlet, NUPDOWN = 0 vs Triplet, NUPDOWN = 2). When the triplet-state systems were considered, collinear spinpolarized calculations were performed. The geometries of all systems were optimized in their appropriate spin multiplet states. After geometry optimization, the band structure of the perovskite n = 1(PyBA)₂PbI₄ system was calculated along the high-symmetry path $(\Gamma - Z - D - B - \Gamma - A - E - Z - C - Y - \Gamma)$ with 20 k-points included between each high-symmetry point (creating 200 irreducible kpoints) (Figure S15). The band structure of (PyBA)₂PbI₄ revealed the direct band gap as the $\Gamma \to \Gamma$ transition.

In order to determine the Marcus theory energetics for calculation of the Gibbs free energy (ΔG) and the reorganization energy (λ), we break down the full pyrene—perovskite model into its components: pyrene ligand layer (Py) and perovskite core (PbI) (see Figure S16). Then, we calculate the subsystem total energies in the appropriate multiplet states to capture the TET process (Tables S6 and S7). The system's initial state is the pyrene ligand in the singlet state, and the perovskite core in the triplet state. The final state after TET is considered the pyrene ligand in the triplet state and the perovskite core in the singlet state. Thus, we calculate the Gibbs free energy (ΔG) as

$$\Delta G = ((PbI)_{\text{singlet geometry}} + (^{3}Py^{*})_{\text{triplet geometry}})$$
$$- ((^{3}PbI^{*})_{\text{triplet geometry}} + (Py)_{\text{singlet geometry}})$$

and the reorganization energy (λ) as

$$\lambda = ((PbI)_{singlet geometry} + (^{3}Py^{*})_{triplet geometry})$$
$$- ((^{3}PbI^{*})_{triplet geometry} + (Py)_{singlet geometry})$$

ASSOCIATED CONTENT

Supporting Information

The Supporting Information is available free of charge at https://pubs.acs.org/doi/10.1021/jacs.4c00236.

Sample characterization, determination of band alignment, details of fittings of time-resolved data, theory and DFT simulations, and supplemental figures (PDF)

AUTHOR INFORMATION

Corresponding Author

Libai Huang — Department of Chemistry, Purdue University, West Lafayette, Indiana 47907, United States; o orcid.org/0000-0001-9975-3624; Email: libai-huang@purdue.edu

Authors

Angana De − Department of Chemistry, Purdue University, West Lafayette, Indiana 47907, United States; orcid.org/0000-0001-7351-5652

Carlos Mora Perez – Department of Chemistry, University of Southern California, Los Angeles, California 90089, United States; Occid.org/0000-0001-8840-5093

Aihui Liang — Davidson School of Chemical Engineering, Purdue University, West Lafayette, Indiana 47907, United States; College of Chemistry and Chemical Engineering, Jiangxi Normal University, Nanchang, Jiangxi 330022, P. R. China; orcid.org/0000-0003-2956-5796

Kang Wang — Davidson School of Chemical Engineering, Purdue University, West Lafayette, Indiana 47907, United States; orcid.org/0000-0002-7178-1225

Letian Dou – Department of Chemistry, Purdue University, West Lafayette, Indiana 47907, United States; Davidson School of Chemical Engineering and Birck Nanotechnology Center, Purdue University, West Lafayette, Indiana 47907, United States; Occid.org/0000-0001-6411-8591

Oleg Prezhdo — Department of Chemistry, University of Southern California, Los Angeles, California 90089, United States; Occid.org/0000-0002-5140-7500

Complete contact information is available at: https://pubs.acs.org/10.1021/jacs.4c00236

Author Contributions

All authors have given approval to the final version of the manuscript.

Notes

The authors declare no competing financial interest.

ACKNOWLEDGMENTS

The optical characterization effort at Purdue was supported by the U.S. Department of Energy, Office of Basic Energy Sciences through award DE-SC0016356. The sample synthesis and preparation at Purdue were supported by the U.S. Department of Energy, Office of Basic Energy Sciences through award DE-SC0022082. The computational work at the University of Southern California was supported by the US National Science Foundation grant CHE-2154367.

■ REFERENCES

- (1) Wu, M.; Congreve, D. N.; Wilson, M. W. B.; Jean, J.; Geva, N.; Welborn, M.; Van Voorhis, T.; Bulović, V.; Bawendi, M. G.; Baldo, M. A. Solid-state infrared-to-visible upconversion sensitized by colloidal nanocrystals. *Nat. Photonics* **2016**, *10*, 31–34.
- (2) Mongin, C.; Garakyaraghi, S.; Razgoniaeva, N.; Zamkov, M.; Castellano, F. N. Direct observation of triplet energy transfer from semiconductor nanocrystals. *Science* **2016**, *351*, *369*–*372*.
- (3) Xia, P.; Raulerson, E. K.; Coleman, D.; Gerke, C. S.; Mangolini, L.; Tang, M. L.; Roberts, S. T. Achieving spin-triplet exciton transfer between silicon and molecular acceptors for photon upconversion. *Nat. Chem.* **2020**, *12*, 137–144.
- (4) Thompson, N. J.; Wilson, M. W.; Congreve, D. N.; Brown, P. R.; Scherer, J. M.; Bischof, T. S.; Wu, M.; Geva, N.; Welborn, M.; Voorhis, T. V.; Bulovic, V.; Bawendi, M. G.; Baldo, M. A. Energy harvesting of non-emissive triplet excitons in tetracene by emissive PbS nanocrystals. *Nat. Mater.* **2014**, *13*, 1039–1043.
- (5) Tabachnyk, M.; Ehrler, B.; Gelinas, S.; Bohm, M. L.; Walker, B. J.; Musselman, K. P.; Greenham, N. C.; Friend, R. H.; Rao, A. Resonant energy transfer of triplet excitons from pentacene to PbSe nanocrystals. *Nat. Mater.* **2014**, *13*, 1033–1038.
- (6) Qin, C.; Matsushima, T.; Potscavage, W. J.; Sandanayaka, A. S. D.; Leyden, M. R.; Bencheikh, F.; Goushi, K.; Mathevet, F.; Heinrich, B.; Yumoto, G.; Kanemitsu, Y.; Adachi, C. Triplet management for efficient perovskite light-emitting diodes. *Nat. Photonics* **2020**, *14*, 70–75.
- (7) Nienhaus, L.; Wu, M.; Geva, N.; Shepherd, J. J.; Wilson, M. W. B.; Bulovic, V.; Van Voorhis, T.; Baldo, M. A.; Bawendi, M. G. Speed Limit for Triplet-Exciton Transfer in Solid-State PbS Nanocrystal-Sensitized Photon Upconversion. *ACS Nano* **2017**, *11*, 7848–7857.

- (8) Wieghold, S.; Bieber, A. S.; VanOrman, Z. A.; Nienhaus, L. Influence of Triplet Diffusion on Lead Halide Perovskite-Sensitized Solid-State Upconversion. *J. Phys. Chem. Lett.* **2019**, *10*, 3806–3811.
- (9) Nienhaus, L.; Correa-Baena, J.-P.; Wieghold, S.; Einzinger, M.; Lin, T.-A.; Shulenberger, K. E.; Klein, N. D.; Wu, M.; Bulović, V.; Buonassisi, T.; Baldo, M. A.; Bawendi, M. G. Triplet-Sensitization by Lead Halide Perovskite Thin Films for Near-Infrared-to-Visible Upconversion. *ACS Energy Lett.* **2019**, *4*, 888–895.
- (10) Hu, H.; Zhao, D.; Gao, Y.; Qiao, X.; Salim, T.; Chen, B.; Chia, E. E. M.; Grimsdale, A. C.; Lam, Y. M. Harvesting Triplet Excitons in Lead-Halide Perovskites for Room-Temperature Phosphorescence. *Chem. Mater.* **2019**, *31*, 2597–2602.
- (11) Skourtis, S. S.; Liu, C.; Antoniou, P.; Virshup, A. M.; Beratan, D. N. Dexter energy transfer pathways. *Proc. Natl. Acad. Sci. U.S.A.* **2016**, *113*, 8115–8120.
- (12) Yost, S. R.; Hontz, E.; Yeganeh, S.; Van Voorhis, T. Triplet vs Singlet Energy Transfer in Organic Semiconductors: The Tortoise and the Hare. *J. Phys. Chem. C* **2012**, *116*, 17369–17377.
- (13) Braun, M.; Tuffentsammer, W.; Wachtel, H.; Wolf, H. C. Pyrene as emitting chromophore in organic-inorganic lead halide-based layered perovskites with different halides. *Chem. Phys. Lett.* **1999**, 307, 373–378.
- (14) Andreasson, J.; Kyrychenko, A.; Martensson, J.; Albinsson, B. Temperature and viscosity dependence of the triplet energy transfer process in porphyrin dimers. *Photochem. Photobiol. Sci.* **2002**, *1*, 111–119.
- (15) Lai, R.; Liu, Y.; Luo, X.; Chen, L.; Han, Y.; Lv, M.; Liang, G.; Chen, J.; Zhang, C.; Di, D.; Scholes, G. D.; Castellano, F. N.; Wu, K. Shallow distance-dependent triplet energy migration mediated by endothermic charge-transfer. *Nat. Commun.* **2021**, *12*, 1532.
- (16) Li, X.; Huang, Z.; Zavala, R.; Tang, M. L. Distance-Dependent Triplet Energy Transfer between CdSe Nanocrystals and Surface Bound Anthracene. *J. Phys. Chem. Lett.* **2016**, *7*, 1955–1959.
- (17) Luo, X.; Han, Y.; Chen, Z.; Li, Y.; Liang, G.; Liu, X.; Ding, T.; Nie, C.; Wang, M.; Castellano, F. N.; Wu, K. Mechanisms of triplet energy transfer across the inorganic nanocrystal/organic molecule interface. *Nat. Commun.* **2020**, *11*, 28.
- (18) Huang, Z.; Xu, Z.; Huang, T.; Gray, V.; Moth-Poulsen, K.; Lian, T.; Tang, M. L. Evolution from Tunneling to Hopping Mediated Triplet Energy Transfer from Quantum Dots to Molecules. *J. Am. Chem. Soc.* **2020**, *142*, 17581–17588.
- (19) He, S.; Lai, R.; Jiang, Q.; Han, Y.; Luo, X.; Tian, Y.; Liu, X.; Wu, K. Engineering Sensitized Photon Upconversion Efficiency via Nanocrystal Wavefunction and Molecular Geometry. *Angew. Chem., Int. Ed. Engl.* **2020**, *59*, 17726–17731.
- (20) Wong, C. Y.; Kim, J.; Nair, P. S.; Nagy, M. C.; Scholes, G. D. Relaxation in the Exciton Fine Structure of Semiconductor Nanocrystals. *J. Phys. Chem. C* **2009**, *113*, 795–811.
- (21) Ema, K.; Inomata, M.; Kato, Y.; Kunugita, H.; Era, M. Nearly perfect triplet-triplet energy transfer from Wannier excitons to naphthalene in organic-inorganic hybrid quantum-well materials. *Phys. Rev. Lett.* **2008**, *100*, 257401.
- (22) Gao, Y.; Shi, E.; Deng, S.; Shiring, S. B.; Snaider, J. M.; Liang, C.; Yuan, B.; Song, R.; Janke, S. M.; Liebman-Pelaez, A.; Yoo, P.; Zeller, M.; Boudouris, B. W.; Liao, P.; Zhu, C.; Blum, V.; Yu, Y.; Savoie, B. M.; Huang, L.; Dou, L. Molecular engineering of organic-inorganic hybrid perovskites quantum wells. *Nat. Chem.* **2019**, *11*, 1151–1157.
- (23) Dai, Q.; Li, H.; Sini, G.; Bredas, J. L. Evolution of the Nature of Excitons and Electronic Couplings in Hybrid 2D Perovskites as a Function of Organic Cation π -Conjugation. *Adv. Funct. Mater.* **2021**, 32, 2108662.
- (24) Lin, Y. L.; Johnson, J. C. Interlayer Triplet Energy Transfer in Dion-Jacobson Two-Dimensional Lead Halide Perovskites Containing Naphthalene Diammonium Cations. *J. Phys. Chem. Lett.* **2021**, *12*, 4793–4798.
- (25) Tian, Y.; Li, Y.; Chen, B.; Lai, R.; He, S.; Luo, X.; Han, Y.; Wei, Y.; Wu, K. Sensitized Molecular Triplet and Triplet Excimer Emission

- in Two-Dimensional Hybrid Perovskites. J. Phys. Chem. Lett. 2020, 11, 2247–2255.
- (26) Zhao, L.; Lin, Y. L.; Kim, H.; Giebink, N. C.; Rand, B. P. Donor/Acceptor Charge-Transfer States at Two-Dimensional Metal Halide Perovskite and Organic Semiconductor Interfaces. *ACS Energy Lett.* **2018**, *3*, 2708–2712.
- (27) Mohan Raj, A.; Sharma, G.; Prabhakar, R.; Ramamurthy, V. Room-Temperature Phosphorescence from Encapsulated Pyrene Induced by Xenon. *J. Phys. Chem. A* **2019**, *123*, 9123–9131.
- (28) Easley, C. J.; Mettry, M.; Moses, E. M.; Hooley, R. J.; Bardeen, C. J. Boosting the Heavy Atom Effect by Cavitand Encapsulation: Room Temperature Phosphorescence of Pyrene in the Presence of Oxygen. J. Phys. Chem. A 2018, 122, 6578–6584.
- (29) peter, L.; Vaubel, G. Phosphorescence of Pure Crystalline Pyrene. *Chem. Phys. Lett.* **1973**, 21, 158–160.
- (30) Van Gompel, W. T. M.; Herckens, R.; Van Hecke, K.; Ruttens, B.; D'Haen, J.; Lutsen, L.; Vanderzande, D. Low-Dimensional Hybrid Perovskites Containing an Organic Cation with an Extended Conjugated System: Tuning the Excitonic Absorption Features. *ChemNanoMat* **2019**, *5*, 323–327.
- (31) Mistelberger, K.; Port, H. The Triplet State in Pyrene. *Mol. Cryst. Liq. Cryst.* **1980**, *57*, 203–226.
- (32) Ferguson, J. Absorption and Fluorescence Spectra of Crystalline Pyrene. J. Chem. Phys. 1958, 28, 765–768.
- (33) Yu, C.; Yam, V. W. Glucose sensing via polyanion formation and induced pyrene excimer emission. *Chem. Commun.* **2009**, 1347–1349.
- (34) Zhao, M.; Zhou, X.; Tang, J.; Deng, Z.; Xu, X.; Chen, Z.; Li, X.; Yang, L.; Ma, L. J. Pyrene excimer-based fluorescent sensor for detection and removal of Fe(3+) and Pb(2+) from aqueous solutions. *Spectrochim. Acta, Part A* **2017**, *173*, 235–240.
- (35) DuBose, J. T.; Christy, A.; Chakkamalayath, J.; Kamat, P. V. Trap or Triplet? Excited-State Interactions in 2D Perovskite Colloids with Chromophoric Cations. *ACS Nano* **2023**, *17*, 19052–19062.
- (36) Gijzeman, O. L. J.; Langelaar, J.; Van Voorst, J. D. W. Triplet Excimer Emission from Pyrene Single Crystals. *Chem. Phys. Lett.* **1970**, *5*, 269–272.
- (37) Zhai, Y.; Baniya, S.; Zhang, C.; Li, J.; Haney, P.; Sheng, C. X.; Ehrenfreund, E.; Vardeny, Z. V. Giant Rashba splitting in 2D organic-inorganic halide perovskites measured by transient spectroscopies. *Sci. Adv.* **2017**, *3*, No. e1700704.
- (38) Do, T. T. H.; Granados Del Aguila, A.; Zhang, D.; Xing, J.; Liu, S.; Prosnikov, M. A.; Gao, W.; Chang, K.; Christianen, P. C. M.; Xiong, Q. Bright Exciton Fine-Structure in Two-Dimensional Lead Halide Perovskites. *Nano Lett.* **2020**, *20*, 5141–5148.
- (39) Posmyk, K.; Zawadzka, N.; Dyksik, M.; Surrente, A.; Maude, D. K.; Kazimierczuk, T.; Babinski, A.; Molas, M. R.; Paritmongkol, W.; Maczka, M.; Tisdale, W. A.; Plochocka, P.; Baranowski, M. Quantification of Exciton Fine Structure Splitting in a Two-Dimensional Perovskite Compound. *J. Phys. Chem. Lett.* **2022**, *13*, 4463–4469.
- (40) Kahmann, S.; Duim, H.; Fang, H. H.; Dyksik, M.; Adjokatse, S.; Rivera Medina, M.; Pitaro, M.; Plochocka, P.; Loi, M. A. Photophysics of Two-Dimensional Perovskites—Learning from Metal Halide Substitution. *Adv. Funct. Mater.* **2021**, *31*, 46.
- (41) Rivera, P.; Schaibley, J. R.; Jones, A. M.; Ross, J. S.; Wu, S.; Aivazian, G.; Klement, P.; Seyler, K.; Clark, G.; Ghimire, N. J.; Yan, J.; Mandrus, D. G.; Yao, W.; Xu, X. Observation of long-lived interlayer excitons in monolayer MoSe2-WSe2 heterostructures. *Nat. Commun.* 2015, *6*, 6242.
- (42) Shafikov, M. Z.; Zaytsev, A. V.; Kozhevnikov, V. N. Halide-Enhanced Spin-Orbit Coupling and the Phosphorescence Rate in Ir(III) Complexes. *Inorg. Chem.* **2021**, *60*, 642–650.
- (43) Lin, Y. L.; Johnson, J. C. Tunable Broadband Molecular Emission in Mixed-Organic-Cation Two-Dimensional Hybrid Perovskites. ACS Appl. Opt. Mater. 2023, 1, 3–9.
- (44) Pan, Y. Y.; Huang, J.; Wang, Z. M.; Yu, D. W.; Yang, B.; Ma, Y. G. Computational investigation on the large energy gap between the triplet excited-states in acenes. *RSC Adv.* **2017**, *7*, 26697–26703.

- (45) Deng, S.; Snaider, J. M.; Gao, Y.; Shi, E.; Jin, L.; Schaller, R. D.; Dou, L.; Huang, L. Long-lived charge separation in two-dimensional ligand-perovskite heterostructures. *J. Chem. Phys.* **2020**, *152*, 044711.
- (46) Takada, T.; Kawai, K.; Tojo, S.; Majima, T. Kinetics of Multistep Hole Transfer in DNA by Monitoring the Transient Absorption of the Pyrene Radical Cation. *J. Phys. Chem. B* **2003**, *107*, 14052–14057.
- (47) Marcus, R. A.; Sutin, N. Electron transfers in chemistry and biology. *Biochim. Biophys. Acta, Rev. Bioenerg.* 1985, 811, 265-322.
- (48) Köhler, A.; Bässler, H. What controls triplet exciton transfer in organic semiconductors? *J. Mater. Chem.* **2011**, 21, 4003–4011.
- (49) Gunner, M. R.; Dutton, P. L. Temperature and --. DELTA.G.degree. dependence of the electron transfer from BPh.cntdot.- to QA in reaction center protein from Rhodobacter sphaeroides with different quinones as QA. J. Am. Chem. Soc. 1989, 111, 3400–3412.
- (50) Yan, H.; Bergren, A. J.; McCreery, R.; Della Rocca, M. L.; Martin, P.; Lafarge, P.; Lacroix, J. C. Activationless charge transport across 4.5 to 22 nm in molecular electronic junctions. *Proc. Natl. Acad. Sci. U.S.A.* **2013**, *110*, 5326–5330.
- (51) Hohenberg, P.; Kohn, W. Inhomogeneous Electron Gas. *Phys. Rev.* **1964**, *136*, B864–B871.
- (52) Kohn, W.; Sham, L. J. Self-Consistent Equations Including Exchange and Correlation Effects. *Phys. Rev.* **1965**, *140*, A1133–A1138.
- (53) Blochl, P. E. Projector augmented-wave method. *Phys. Rev. B: Condens. Matter Mater. Phys.* **1994**, *50*, 17953–17979.
- (54) Wang, J.; Ding, T.; Gao, K.; Wang, L.; Zhou, P.; Wu, K. Marcus inverted region of charge transfer from low-dimensional semi-conductor materials. *Nat. Commun.* **2021**, *12*, 6333.
- (55) Marcus, R. A. Exchange reactions and electron transfer reactions including isotopic exchange. Theory of oxidation-reduction reactions involving electron transfer. Part 4.—A statistical-mechanical basis for treating contributions from solvent, ligands, and inert salt. *Discuss. Faraday Soc.* **1960**, *29*, 21–31.
- (56) Shuai, Z.; Li, W.; Ren, J.; Jiang, Y.; Geng, H. Applying Marcus theory to describe the carrier transports in organic semiconductors: Limitations and beyond. *J. Chem. Phys.* **2020**, *153*, 080902.
- (57) Dakhnovskii, Y. I.; Doolen, R.; Simon, J. D. Electron transfer in the Marcus inverted region: Experiment and adiabatic tunneling mechanism. *J. Chem. Phys.* **1994**, *101*, 6640–6647.
- (58) Yin, Z.; Leng, J.; Wang, S.; Liang, G.; Tian, W.; Wu, K.; Jin, S. Auger-Assisted Electron Transfer between Adjacent Quantum Wells in Two-Dimensional Layered Perovskites. *J. Am. Chem. Soc.* **2021**, 143, 4725–4731.
- (59) Perdew, J. P.; Burke, K.; Ernzerhof, M. Generalized Gradient Approximation Made Simple. *Phys. Rev. Lett.* **1996**, 77, 3865–3868.
- (60) Perdew, J. P.; Burke, K.; Wang, Y. Generalized gradient approximation for the exchange-correlation hole of a many-electron system. *Phys. Rev. B* **1996**, *54*, 16533–16539.
- (61) Kresse, G.; Hafner, J. Ab initio molecular dynamics for liquid metals. *Phys. Rev. B: Condens. Matter Mater. Phys.* **1993**, 47, 558–561.
- (62) Kresse, G.; Hafner, J. Ab initio molecular-dynamics simulation of the liquid-metal-amorphous-semiconductor transition in germanium. *Phys. Rev. B: Condens. Matter Mater. Phys.* **1994**, 49, 14251–14269.
- (63) Kresse, G.; Furthmüller, J. Efficiency of ab-initio total energy calculations for metals and semiconductors using a plane-wave basis set. *Comput. Mater. Sci.* **1996**, *6*, 15–50.
- (64) Grimme, S.; Ehrlich, S.; Goerigk, L. Effect of the damping function in dispersion corrected density functional theory. *J. Comput. Chem.* **2011**, 32, 1456–1465.

☐ Recommended by ACS

Nonvolatile Modulation of Light Emission from Delocalized and Defect-Bound Excitons in Monolayer MoS₂ Using the Remnant Polarization in the Ferroelectric Polymer P(VD...

Joon-Seok Kim, Lincoln J. Lauhon, et al.

SEPTEMBER 27, 2023

ACS APPLIED NANO MATERIALS

READ 🗹

Robustness of Trion State in Gated Monolayer MoSe₂ under Pressure

Zeya Li, Hongtao Yuan, et al.

OCTOBER 31, 2023

NANO LETTERS

READ 🗹

Bipolaronic Nature of the Pseudogap in Quasi-One-Dimensional (TaSe₄), I Revealed via Weak Photoexcitation

Yingchao Zhang, Margaret Murnane, et al.

SEPTEMBER 08, 2023

NANO LETTERS

READ 🗹

"Dead" Exciton Layer and Exciton Anisotropy of Bulk MoS₂ Extracted from Optical Measurements

Vasyl G. Kravets, Alexander N. Grigorenko, et al.

NOVEMBER 09, 2022

ACS NANO

READ 🗹

Get More Suggestions >